

A benchmark for multi-conjugated AO: VLT–MAD observations of the young massive cluster Trumpler 14 ^{*}

B. Rochau^{1†}, W. Brandner¹, A. Stolte², T. Henning¹, N. Da Rio^{1,3},
M. Gennaro¹, F. Hormuth¹, E. Marchetti⁴ and P. Amico⁴

¹*Max-Planck-Institut für Astronomie, Königstuhl 17, 69115 Heidelberg*

²*Argelander Institut für Astronomie, Universität Bonn, Auf dem Hügel 71, 53121 Bonn*

³*Space Telescope Science Institute, 3700 San Martin Drive, Baltimore, MD 21218*

⁴*European Southern Observatory, Karl-Schwarzschild-Straße 2, 85748 Garching bei München*

Accepted 2011 July 30. Received 2011 July 30; in original form 2011 May 8

ABSTRACT

MAD is the first multi-conjugated adaptive optics system at the VLT. We present H and K_S observations of the young massive cluster Trumpler 14 revealing the power of MCAO systems by providing a homogeneous Strehl ratio over a large field of view. Mean Strehl ratios of 6.0 and 5.9 per cent with maximum Strehl ratios of 9.8 and 12.6 per cent in H and K_S , respectively, show significant improvement of the spatial PSF stability compared to single-conjugated adaptive optics systems. Photometry of our observations cover a dynamic range of ~ 10 mag including 2–3 times more sources than comparable seeing-limited observations. The colour-magnitude diagram reveals that the massive cluster originated in a recent starburst-like event 1 ± 0.5 Myr ago. We tentatively detect hints for an older population of 3 Myr suggesting that low intensity star formation might have been going on in the HII region for a few Myr. We derive the luminosity function and mass function between $0.1 M_\odot$ and $3.2 M_\odot$ and identify a change of the power law slope of the mass function at $m_c \sim 0.53^{+0.12}_{-0.10} M_\odot$. The MF appears shallow with power law slopes of $\Gamma_1 = -0.50 \pm 0.11$ above m_c and $\Gamma_2 = 0.63 \pm 0.32$ below m_c .

Key words: Instrumentation: adaptive optics – (Galaxy:) open clusters and associations: individual: Trumpler 14 – Stars: pre-main sequence

1 INTRODUCTION

Adaptive optics (AO) systems have proven their outstanding ability in compensating atmospheric seeing over more than 20 years. With the first common user AO system, ADONIS, mounted at the ESO 3.6m telescope on La Silla (Rousset et al. 1990), ground-based telescopes provide observations with previously unachieved angular resolution. However, the performance of a single-conjugated AO (SCAO) system is restricted to small fields of view (FoV). With typical isoplanatic angles of 15 arcsec, the AO performance degrades quickly at distances of 20–30 arcsec from the guide star (GS). Thus, AO assisted observations are limited to maximum field sizes of ~ 1 arcmin with good AO corrections for a typical FoV of 30 arcsec. To provide

a spatially more stable performance, multi-conjugated AO (MCAO) systems are required. MCAO uses several GSs to correct the blurring due to Earth’s atmosphere. In the framework of second generation instruments for the VLT and the E-ELT, the Multi-conjugate Adaptive optics Demonstrator (MAD), was developed in 2007 as the first MCAO system at the VLT (Marchetti et al. 2003, 2004, 2007).

The proximity of the Carina Nebula and its cluster population provides an ideal testbed to assess the capability of VLT–MAD. The combination of high spatial resolution and the wide field of VLT–MAD allows to resolve the dense central regions of the clusters. NGC 3372, or Carina Nebula, is a Galactic giant molecular cloud and a site of vigorous and ongoing star formation including several young massive clusters. It includes not only dozens of young O- and B-type stars but also evolved Wolf–Rayet stars (e.g. Massey & Johnson 1993). The youngest and most populous clusters of the region are the open clusters Trumpler 14 and Trumpler 16 (hereafter Tr 14 and Tr 16), located in the central part of the Carina Nebula. The high-

^{*} Based on Observations with VLT–MAD collected during the Science Verification campaign at the European Southern Observatory, Paranal, Chile.

[†] E-mail: rochau@mpia.de

Table 1. Strehl values over the 1×1 arcmin FoV

Origin	Filter	max. Strehl	min. Strehl	mean Strehl
Obs. MCAO	H	9.8 %	3.3 %	6.0 %
Obs. MCAO	K_S	12.6 %	1.3 %	5.9 %
Sim. SCAO	H_{sim}	9.8 %	< 0.01 %	1.6 %
Sim. SCAO	$K_{S,sim}$	12.6 %	< 0.01 %	2.0 %

mass population with its strong UV radiation interacts with the surrounding material triggering subsequent star formation (e.g. Rathborne et al. 2002). The stellar population of Tr 14 includes several O-type stars, notably the O2If* star HD93129Aa (Walborn et al. 2002) which has been found to be the most massive star in Tr 14 with an estimated mass in excess of $100 M_{\odot}$ (Nelan et al. 2004). Assuming a Kroupa-IMF, Tr 14 was suggested to be as massive as a few $10^3 M_{\odot}$ (Sana et al. 2010), which puts it close to the regime of the Galactic starburst clusters like NGC 3603 YC or the Arches Cluster (e.g. Rochau et al. 2010; Stolte et al. 2002, resp.). The Carina Nebula is the closest region harboring such a massive young cluster, with recent studies estimating the distance of Tr 14 to be between ~ 2 and 3 kpc (e.g. Tapia et al. 2003; Carraro et al. 2004; Ascenso et al. 2007). The lack of evolved stars makes Tr 14 a very young cluster. The ages of the high-mass content of Tr 14 and Tr 16 are estimated to be around 1 – 2 Myr (Vazquez et al. 1996) and 2 – 3 Myr (Smith 2006), respectively, while the formation of intermediate-mass stars probably started earlier. This is supported by the core-halo structure of the cluster, with the halo being slightly older (Ascenso et al. 2007). However, the ages of the clusters as well as the distance estimates remain controversial. One reason could be the anomalous extinction law towards the clusters (e.g. Tapia et al. 2003), as this hampers precise age determinations, masking uncertainties/differences in the models for low- and high-mass stars in the main sequence and pre-main sequence, respectively (Naylor 2009).

We were able to obtain MCAO assisted observations with VLT-MAD to investigate the young massive star cluster Tr 14 (PIs: H. Sana, B. Rochau). In 2010, Sana et al. presented their analysis of the data of the entire $2 \text{ arcmin} \times 2 \text{ arcmin}$ FoV. Their scientific focus was on deriving the colour-magnitude diagram (CMD), structure of the cluster and to conduct a companion analysis. In contrast, our aim is the investigation of the pre-main sequence population down to its low- and very-low mass members and the underlying mass function. Therefore, we concentrate on the deeper H - and K_S -band observations of the central 1 arcmin^2 of the cluster. The results of our investigation are presented as follows: In Sect. 2 we introduce shortly the MCAO system MAD, followed by the description of the observations and the data reduction (Sect. 3). Sect. 4 includes a technical analysis of the MCAO performance. The scientific analysis is presented in Sect. 5 and our results are summarised in Sect. 6.

2 VLT-MULTI-CONJUGATE ADAPTIVE OPTICS DEMONSTRATOR

MAD has been developed as the first prototype MCAO system for the VLT. It aims at demonstrating the feasibility of MCAO systems in general and to investigate different reconstruction techniques in particular.

MAD is designed to correct for blurring due to atmospheric turbulence over 2 arcmin on the sky using Natural Guide Stars (NGS). Two Deformable Mirrors are used for the MCAO correction. The first, optically conjugated at the telescope pupil, corrects for the ground layer turbulence, while the second, conjugated at 8.5 km elevation above the telescope, corrects for the field anisoplanatism.

To examine the differences between the star- and layer-oriented reconstruction technique, two different wavefront sensors (WFS) are installed. The star-oriented MCAO correction is supported by a Multi Shack-Hartmann WFS. The layer-oriented MCAO reconstruction uses a Layer Oriented Multi-Pyramid WFS. Both WFSs can sense simultaneously several NGS at visual wavelength but only one mode will be used at a time. Our observations were processed in star-oriented mode using 3 NGS.

MAD is equipped with the IR camera CAMCAO (CAmera for MCAO) providing near-infrared broad- and narrow-band imaging, using a HAWAII2 $2k \times 2k$ HgCdTe detector. With an image scale of $0.028 \text{ arcsec pixel}^{-1}$, the camera covers a $59 \text{ arcsec} \times 59 \text{ arcsec}$ FoV (Amorim et al. 2006). A $2 \text{ arcmin} \times 2 \text{ arcmin}$ FoV can be covered by moving the camera while the telescope is tracking and the AO loop remains closed. In contrast to SCAO, using multiple GSs allows to cover a larger AO corrected FoV with homogeneous Strehl ratios.

3 OBSERVATIONS AND DATA REDUCTION

3.1 Observations

Observations were carried out during the night of 2008, January 12 by the VLT-MAD team. Deep H and K_S images were taken to map the innermost region of the young massive cluster Tr 14 ($\alpha = 10^{\text{h}}43^{\text{m}}55^{\text{s}}$, $\delta = -59^{\circ}33'03''$). Short integration times of 2 s were used to avoid severe saturation, and 30 individual integrations are co-added to a single exposure of 1 min . Raw data reduction and image combination was performed using the ESO image processing software *Eclipse* (Devillard 2001). For sky and dark subtraction as well as for flat field correction the calibration images taken during the science run are used. The sky and dark current subtracted, flat field corrected images are subsequently combined using the shift-and-add tool of *Eclipse*. 28 single exposures of 1 min in each band are combined to a single frame of 28 min

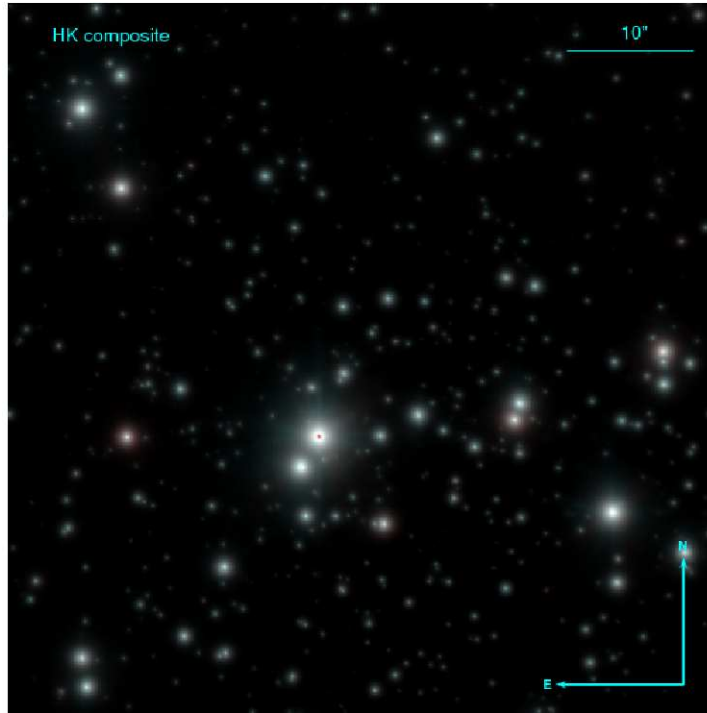


Figure 1. Central region of Tr 14 as seen with VLT–MAD (north is up, east to the left). This HK_S colour composite shows the densest region of the cluster including the most massive cluster member HD93129Aa ($\alpha = 10^{\text{h}}43^{\text{m}}57.5^{\text{s}}$, $\delta = -59^{\circ}32'52.3''$) as the brightest star in the field.

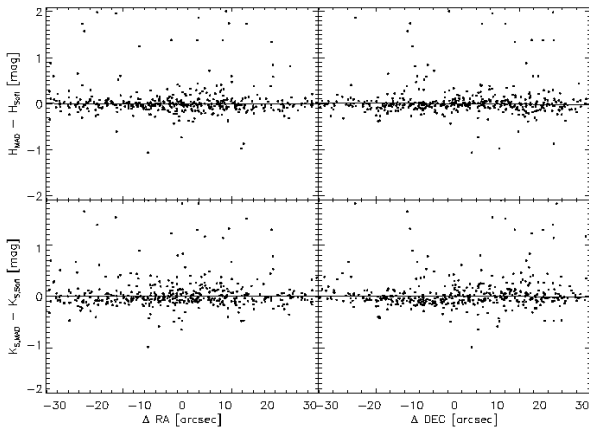


Figure 2. Observed differences between the MAD and the NTT–SofI photometry after application of the constant ZP correction. ZP offsets are measured and plotted as a function of right ascension (left panels) and declination (right panels) for the H -band (upper panels) and K_S -band (lower panels). Straight lines show the linear fit to the observed distribution revealing the spatial stability of the photometry.

of total integration time. For comparison, the observations of the adjacent fields provided only 8 min of total exposure time (see also Table 2 of Sana et al. 2010). The final FoV of the central field covers an area of $68 \text{ arcsec} \times 68 \text{ arcsec}$, and the HK_S colour composite is shown in Fig. 1. Located close to the centre is HD93129Aa, the most massive member and brightest star in the field.

3.2 Photometry

To study the stellar content of Tr 14, we perform PSF photometry using IRAF/DAOPHOT (Stetson 1990). Fitting 15 stars in H - and K_S -band, we find a Penny-PSF, comprising a Gaussian kernel and Lorentzian wings, as the best-fitting PSF. It further turns out that a second order variable PSF provides a good match to the MAD data obtained with the star-oriented mode. Photometric calibration is based on NTT–SofI observations of Tr 14 published by Ascenso et al. (2007). The detectors and filter systems of MAD and NTT–SofI are similar, leading to the absence of e.g. colour terms. Consequently, using the photometric catalogue of the MAD and NTT–SofI observations is well suited to assess the goodness of the PSF characterization of our MCAO observations.

The comparison of seeing-limited NTT–SofI photometry with our MAD photometry reveals no trend of photometric zeropoint (ZP) with position on the MAD field ($\sim 1.1 \text{ arcmin} \times 1.1 \text{ arcmin}$) and shows a rms scatter of 0.11 mag in H -band and 0.12 mag in K_S -band, respectively (Fig. 2). Furthermore, Fig. 4 displays the ZP offset to be also constant with magnitude and colour. This agrees very well with the results of Sana et al. (2010) who applied PSF photometry to individual frames of 1 min instead of the combined image as used in our analysis. The spatially stable photometry emphasises that the stability of the PSF is comparable to that of seeing-limited observations, and exceeds the stability of SCAO imaging, where anisoplanatic effects result in considerably larger variations in the PSF across the FoV.

Thus, the combination of star-oriented MAD observations with a second order variable PSF yields high precision photometry across the entire FoV. The final photometric catalogue includes 1347 stars. Excluding stars with

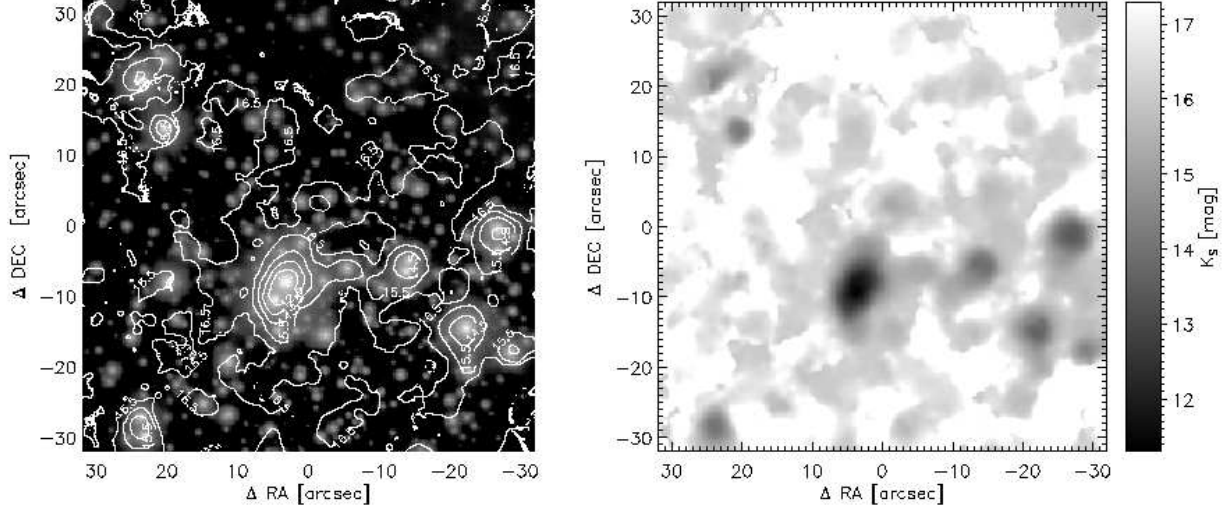


Figure 3. K_S -band completeness map of Tr 14. *Left Panel:* K_S -band image of Tr 14, north is up and east to the left. Magnitudes at which 70 per cent completeness is achieved are superimposed as white contours (in steps of 1 mag). The image is centered (0/0) at $\alpha = 10^{\text{h}}43^{\text{m}}57.2^{\text{s}}$, $\delta = -59^{\circ}32'44.2''$. *Right Panel:* K_S -band completeness map of the entire observed FoV. The grey shades correspond to the K_S -band magnitude at which a completeness of 70 per cent is achieved. The strong local decrease of completeness close to bright stars without displaying large scale variations across the field shows that crowding effects are less important compared to the possible faintness of the stars.

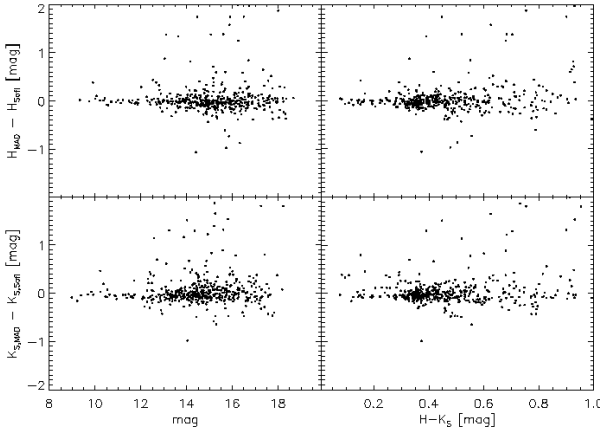


Figure 4. Observed differences between the MAD and the NTT-SofI photometry after application of the constant ZP correction as a function of magnitude (left panels) and colour (right panels) for the H -band (upper panels) and K_S -band (lower panels).

DAOPHOT photometric uncertainties above 0.1 mag (375 sources), we used a catalogue of 972 stars for the further analysis comprising stars over a dynamic range of ~ 10 mag. Comparison to the 453 sources detected with NTT-SofI in the MAD field shows that VLT-MAD was able to detect 2-3 times as many sources.

3.3 Completeness

We aim at deriving the luminosity function (LF) and, subsequently, the mass function (MF) of Tr 14. To derive the correct cluster LF and MF, accurate knowledge of the com-

pleteness of the photometric catalogue is required. In dense stellar fields the detectability of a source depends on its flux and the local stellar density ('crowding'), and thus, on brightness and position of the source in the observed field. Crowding describes the effect of a decreasing detection probability due to high stellar densities in the sense that a high brightness contrast between a point source and a possible bright neighbour limits its detectability.

To determine the completeness, we apply the same technique as described in Gennaro et al. (2011). We will briefly summarise the procedure here and refer to the Appendix of Gennaro et al. (2011) for further details. Artificial stars are inserted at random positions in the field, and the data analysis is re-run to estimate the fraction of recoveries. We added 50 artificial stars per run to our science image using the PSF derived with DAOPHOT. The rather low number of artificial stars has been chosen in order to not change the crowding characteristics of the observations. 100 individual runs are processed to add a total of 5,000 stars to our image in each photometric bin of 0.5 mag width. We achieve a typical separation between simulated stars of $d_{sim} \sim 34$ pixel.

The final product of our procedure for each photometric band 'j' is the completeness as a function of position on the detector and magnitude of the star:

$$C_j(x, y, \mu) = \frac{\alpha(x, y)}{\exp\left(\frac{\mu - \beta(x, y)}{\gamma(x, y)}\right) + 1} \quad (1)$$

Here μ is the magnitude of the corresponding star, α (≤ 1) is the normalization factor, β the magnitude at which the completeness is $\alpha/2$, and γ describes how fast the completeness C_j drops to zero with decreasing brightness. With the derived values for (α, β, γ) , we can assign a completeness factor to each star considering its magnitude and position.

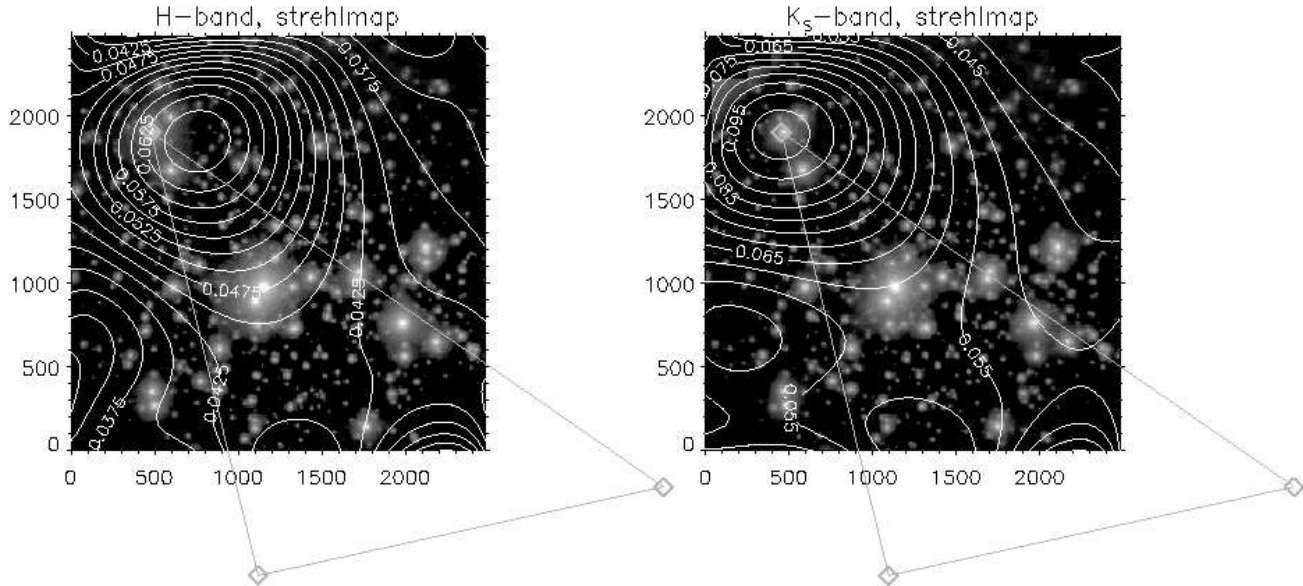


Figure 5. H- and K_S -band image of the core of Tr 14 (left and right panel, respectively). North is up and east is to the left. Overplotted contours show the level of equal Strehl ratios in H - and K_S -band. Apparent is the smooth decrease of Strehl values with the peak value centered on the GS included in the field in the K_S -band. The offset of the peak Strehl to the position of the GS in the H -band is an artefact caused by the saturation of the star. Positions of the GSs are indicated by the grey diamonds and the encircled triangle by the straight grey lines.

Fig. 3 shows the K_S -band image of Tr 14 with the 70 per cent completeness limits at different magnitudes superimposed as contours (left panel). The right panel depicts the same completeness limits over the field as a function of magnitude. The limiting magnitude is significantly brighter in the proximity of the brightest stars. In less dense areas with fainter stars the completeness shows a smooth distribution over the field with a rather faint average limiting magnitude. In addition with the proximity of the cluster, this reveals that crowding is not a major source of incompleteness compared to the stellar faintness. Together with the largely increased number of detections when compared to the seeing-limited NTT-SofI observations, this illustrates the improved performance provided by MAD.

4 TECHNICAL ANALYSIS

The observations have been carried out under observing conditions with a typical seeing between 0.7 and 1.6 arcsec. The MCAO correction provide data with an average full width at half maximum (FWHM) of 0.22 and 0.26 arcsec in H - and K_S -band, respectively. The relatively bad seeing conditions, under which the observation were accomplished, hampered a better correction. Considering the good geometry and brightness of the GSs together with good seeing conditions allow MAD to easily achieve AO corrections down to a FWHM of 0.15 arcsec, or even below (e.g. Momany et al. 2008; Campbell et al. 2010). Seeing-limited NTT-SofI observations of Tr 14 by Ascenso et al. (2007) had, for comparison, a FWHM around 0.7 arcsec.

To investigate the performance of the MCAO system

we measure the Strehl ratio of the combined image across the field. It is defined as the ratio of the measured peak intensity to the peak intensity of an ideal diffraction-limited image of a star of equal magnitude. Stellar properties are extracted from the combined images using the Source Extractor software (Bertin & Arnouts 1996). The theoretical diffraction-limited PSF is created with the *imgen* task in the *Eclipse* package, using a primary and secondary mirror aperture of 8.2 and 1.1 m, respectively, a central wavelengths of $\lambda_H = 1.65 \mu\text{m}$ and $\lambda_{K_S} = 2.125 \mu\text{m}$, with a width of $\Delta\lambda_H = 0.3 \mu\text{m}$ and $\Delta\lambda_{K_S} = 0.35 \mu\text{m}$. We derive the Strehl ratios of our H - and K_S -band observations and the distributions of Strehl ratios in H - and K_S -band over the observed FoV are shown in Fig. 5 as white contours. As expected in the star-oriented mode of MAD, the Strehl ratio is maximised on the GS. Maximum Strehl values of 9.8 per cent (H -band) and 12.6 per cent (K_S -band) are measured. The Strehl map, furthermore, reveals a shallow decrease of the Strehl ratio over the FoV. This is indicated by mean Strehl ratios of 6.0 per cent for H -band and 5.9 per cent for K_S -band. The results are summarised in Table 1. A steep decrease of the AO performance, as observed in SCAO observations, is alleviated due to the decreasing distance towards the other two GSs which are located outside our FoV.

To quantify the difference between MCAO and SCAO, we compare our observations to simulated SCAO observations. We create a grid representing our observed MAD FoV and assign values of Strehl ratios to each grid element with maximum Strehl ratios at the GS location according to our observations. The spatial variation of the Strehl ratio is assumed to follow $SR = S_0 \exp(-[\frac{\Delta\theta}{\theta_{iso}}]^{5/3})$ (Cresci et al. 2005) with S_0 as the maximum Strehl ratio and an isoplanatic

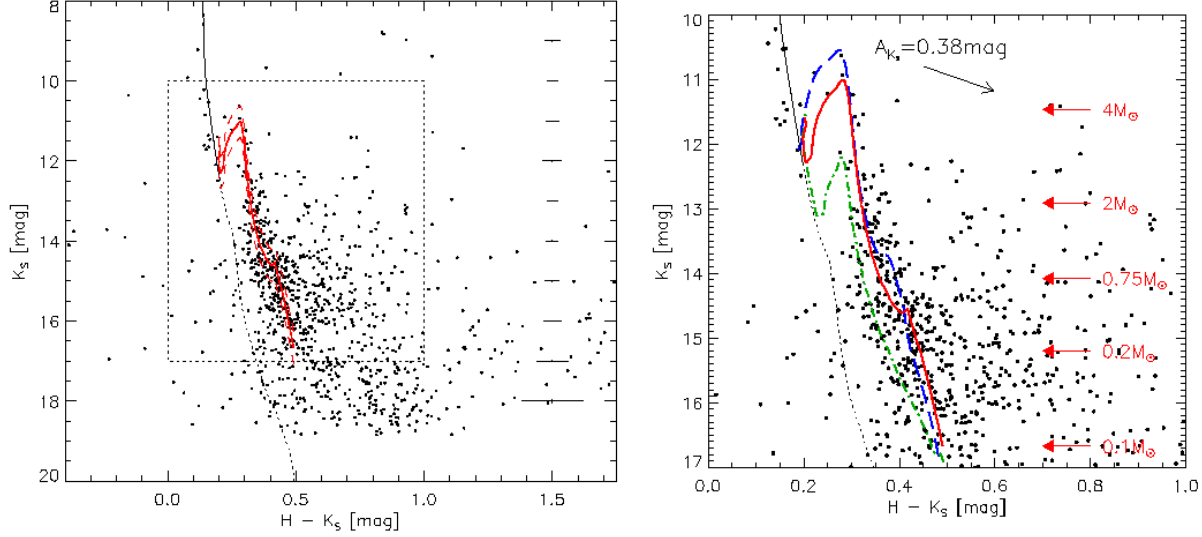


Figure 6. K_S vs. $H - K_S$ CMD of the central 0.75 pc of Tr 14. The cluster population can be identified as the well populated PMS in the CMD and goes down to (and beyond) the H-burning limit. *Left Panel:* The CMD is well represented by a Siess isochrone of 1 Myr in age (red solid line); red dashed lines show the uncertainties in the distance modulus. The MS isochrone is shown by the thin and the dotted black line. The box (dotted lines) displays the region that is shown in the right panel. *Right Panel:* The CMD with the 0.5 Myr, 1 Myr and 3 Myr Siess isochrones overplotted (blue dashed, red solid and green dash-dotted line, respectively). Labelled masses are taken from the 1 Myr Siess isochrone.

angle $\Theta_{\text{iso}} = 15$ arcsec as a typical value for SCAO observations. Results of the simulations are also summarised in Table 1. We found mean Strehl values of 1.6 and 2.0 per cent for the H - and K_S -band, respectively. The larger mean Strehls in our MAD observations reveal the improved spatial stability of the PSF in our MCAO observations compared to SCAO imaging.

Although SCAO observations provide higher peak Strehl ratios, the fastly decreasing performance with distance to the GS makes a good characterization of the PSF at larger distances difficult. Especially in crowding-limited regions, such as dense stellar clusters, this hampers the census of the stellar population. The greater homogeneity of the PSF provided by MCAO observations allows, therefore, the coverage of larger AO corrected areas on the sky, crucial for photometric and astrometric studies of extended stellar populations.

5 SCIENTIFIC ANALYSIS

5.1 Colour-magnitude diagram

Using the photometry of Sect. 3.2, we create a K_S vs. $H - K_S$ CMD, shown in Fig. 6. The CMD allows the identification of the cluster population, primarily the cluster pre-main sequence (PMS) population between $10 \text{ mag} < K_S < 16 \text{ mag}$ and $0.2 \text{ mag} < H - K_S < 0.5 \text{ mag}$. The transition region from PMS to the main sequence (MS) is sparsely populated but can be identified at $10.5 \text{ mag} < K_S < 12.5 \text{ mag}$ with $0.1 \text{ mag} < H - K_S < 0.3 \text{ mag}$. Stars redder than the PMS ($H - K_S \gtrsim 0.5 \text{ mag}$) suffer either from severe differential extinction in the region, are background objects, highly reddened by the Carina Nebula or belong to the cluster as PMS stars surrounded by circumstellar material such as a disc causing the K_S -band excess.

Without a comparison field, we cannot precisely quantify the contaminating fore- and background field star population and, hence, subtract statistically the contaminating field. However, the identification of different features of the cluster in the CMD (PMS, PMS-MS transition region) still allows the comparison with stellar evolutionary models. For the PMS, we use Siess tracks (Siess et al. 2000), computed as in Da Rio et al. (2009), using the BT-Settl Grid of Allard et al. (2010). MS isochrones are from Marigo et al. (2008). Isochrones that resemble best the observed features are shown in the right panel of Fig. 6 superimposed onto the CMD. The shape and width of the PMS-MS transition has proven to be a good age estimator (e.g. Brandner et al. 2008; Rochau et al. 2010), but in the case of Tr14 the region is sparsely populated. Hence, to estimate the age of the cluster we use the colour difference between the MS and the PMS as well as the shape of the PMS. We identify the cluster PMS as best represented by the 1 Myr isochrone indicating that Tr 14 is a very young stellar population. The derived distance modulus ($DM = 11.8 \pm 0.4 \text{ mag}$) corresponds to a distance of $\sim 2.3 \pm 0.4 \text{ kpc}$. The uncertainty is estimated by finding the closest and farthest distance which gives an acceptable approximation of the PMS of the cluster. The extinction was simultaneously derived to $A_{K_S} = 0.38 \pm 0.03 \text{ mag}$, using $R_V = 4.16$ (Carraro et al. 2004) and the relation of visual and near-infrared extinction according to Cardelli et al. (1989). The error on the average extinction is estimated by shifting the isochrone towards the blue and red boundary of the upper PMS, respectively.

The distance of 2.3 kpc is comparable, though slightly smaller, to earlier derived distance estimates. For example, Carraro et al. (2004) locates Tr 14 at a distance of 2.5 kpc, while Tapia et al. (2003) estimated a somewhat larger distance of 2.63 kpc. Comparing our extinction estimate,

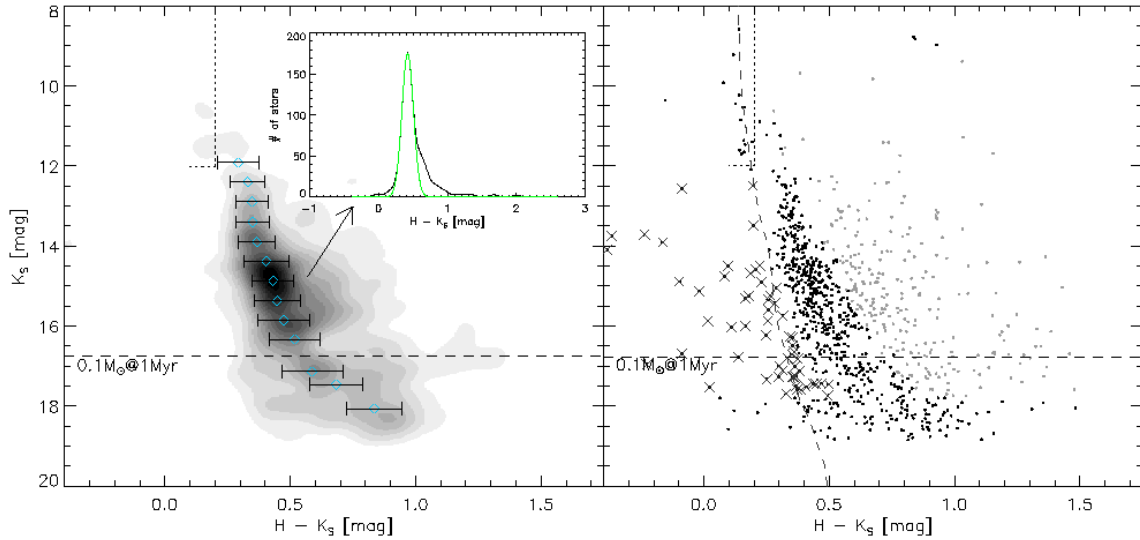


Figure 7. *Left Panel:* Hess diagram based on our photometric catalogue. To distinguish the PMS stars without infrared excess from the contaminating field population and excess sources in the CMD we cut the Hess diagram into stripes of 0.5 mag in magnitude. Blue diamonds show the central magnitude of each stripe (y-axis) and the colour of the peak of the underlying stellar density (x-axis). The errors bars show the 1σ -deviation from the fitted Gaussian function. PMS stars without significant infrared excess are identified by being inside the 1.5σ limit. *Inlay Panel:* An example of the density distribution for one magnitude bin (here: $14.6 \text{ mag} < K_S < 15.1 \text{ mag}$). The black line shows the stellar density as a function of colour. A Gaussian function is fitted around the peak of the distribution and overplotted as the green line. *Right Panel:* The CMD as in Fig. 6 with the identified field contaminants and ‘excess’ sources highlighted (crosses and grey dots, respectively). The field contamination has been excluded while deriving the LF of Tr 14 while the ‘excess’ population is considered. Dotted lines mark the region of the excluded MS population. The dashed line is the 1 Myr MS isochrone by Marigo et al. (2008) and nicely displays the good identification of the field contaminants.

which corresponds to an $A_V = 3.0 \pm 0.4$ mag following the applied extinction law, reveals a slightly higher average extinction towards Tr 14 compared to earlier values, e.g. $A_V = 2.6 \pm 0.2$ mag (Tapia et al. 2003) or $A_V = 2.0 \pm 0.2$ mag (Carraro et al. 2004). We benefit from a higher angular resolution, and the improved photometry might explain the slight differences observed in the different studies.

The best fitting values, distance = 2.3 ± 0.4 kpc and $A_{K_S} = 0.38 \pm 0.03$ mag, are derived using a 1 Myr PMS isochrone. This isochrone fits the PMS-MS colour width and shape of the PMS best. With a different combination of distance and extinction (distance = 2.6 ± 0.4 kpc, $A_{K_S} = 0.36 \pm 0.03$ mag), a slightly younger isochrone (0.5 Myr) represents the PMS-MS colour difference well, but the PMS shape is less well reproduced (Fig. 6). For the 2 Myr isochrone the colour difference between MS and PMS is very narrow compared to the observations. We therefore adopt an uncertainty of 0.5 Myr on the age. However, very young stellar ages should be dealt with carefully as evolutionary models have large uncertainties for ages $\lesssim 1$ Myr, given the strong dependence of the predicted luminosities and temperatures on the initial conditions of the computation (e.g. Baraffe et al. 2002).

Comparing the CMD with the Siess isochrones, we find the 1 Myr isochrone to best resemble the PMS. However, at $14 \text{ mag} < K_S < 16 \text{ mag}$ we identify a number of stars with colours bluer than the isochrone. Apart from observational biases such as photometric uncertainties or a possible lower extinction of the identified sources compared to the derived average extinction, the observed sequence could alternatively be explained by a somewhat older population

of PMS stars. By superposition, we observe that a 3 Myr isochrone nicely follows this blue sequence (see Fig. 6). An older population would support earlier statements of continuous star formation in the Carina Nebula, creating a surrounding older halo population with ages up to 5 Myr (Ascenso et al. 2007).

5.2 Luminosity function

5.2.1 Selection of different populations

Since the observations have been carried out without observing a comparison field, the isolation of the cluster population remained challenging. In order to get a better idea of the cluster population we apply the following approach: We create a Hess diagram based on our H - and K_S -band observations (left panel of Fig. 7) which shows the stellar density in the colour–magnitude plane rather than the single stars.

The Hess diagram is divided into 20 stripes, 0.5 mag wide. In each stripe we examine the stellar density as a function of colour. An example of such a distribution is shown in the inlay diagram in Fig. 7. Around each peak we find a rather symmetric distribution which is well represented by a Gaussian function (peak positions are highlighted as blue diamonds in Fig. 7). The best-fitting Gaussian function is shown by the green line superimposed to the stellar density distribution. 1σ deviations from the peak are plotted as horizontal error bars. The sparsely populated cluster MS yields unreliable fits. Hence, we excluded sources with $K_S < 12 \text{ mag}$ and $H - K_S < 0.2 \text{ mag}$ (dotted lines in Fig. 7). This does not change our results, as we intend to focus in the present work on the PMS population. Thus, we aim to

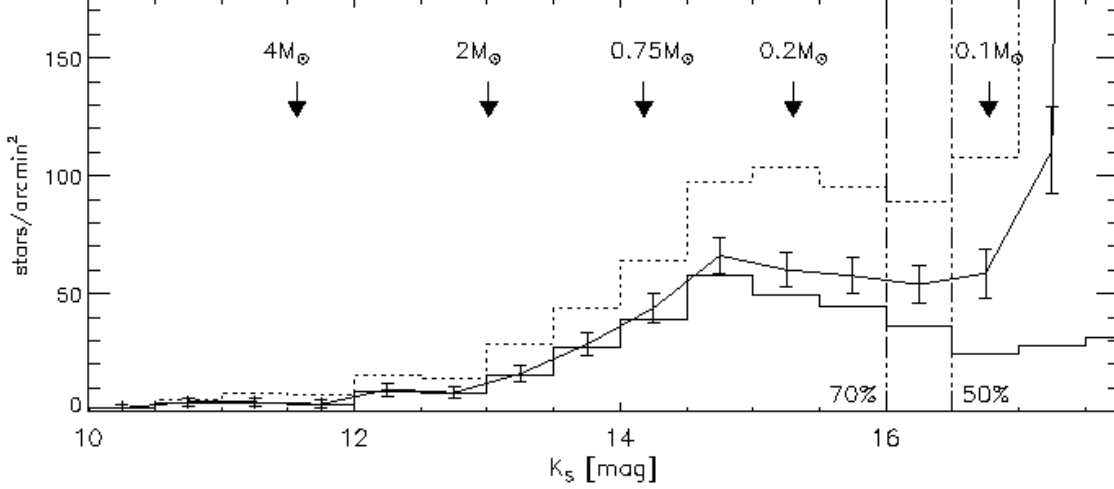


Figure 8. K_S -band LF of Tr 14. Displayed is the number of stars found in magnitude bins of 0.5 mag normalised to the observed area. The histogram shows the number of detected sources while the solid line depicts the same number but corrected for incompleteness. The dashed histogram is the completeness corrected LF including also 'excess' sources. The errors are the Poisson errors of each bin. Corresponding masses, highlighted by the arrows are taken from the 1 Myr Siess isochrone. The LF shows an increasing number of stars with decreasing magnitude to a turnover observed in the $0.25 - 0.54 M_{\odot}$ bin (PMS) and/or in the $0.18 - 0.25 M_{\odot}$ bin (PMS+'excess' sources). The dash-dotted lines mark the limit at which the completeness reaches 50 per cent and 70 per cent, respectively.

isolate the PMS stars without infrared excess from lower mass MS stars belonging to the region but not to the young cluster and foreground sources, for simplicity in the following together called field contamination, as well as from the sources with K_S -band excess. Comparison of the Hess diagram with the CMD reveals that a limiting deviation of 1.5σ divides best the different populations. Sources being off the peak by more than 1.5σ are considered as field contamination (bluer than peak) or as 'excess' cluster sources (redder than the peak) and displayed by the crosses and grey dots in the right panel of Fig. 7, respectively. The limit has been chosen such that stars which can be clearly assigned to the contaminating field are separated from the PMS of the cluster. The PMS is nicely confined along a relatively narrow sequence and the chosen limit provides a good division of the PMS sources into a non-excess and an excess sequence.

Although we cannot clearly identify the origin of the observed excess, these stars are considered as excess sources of the cluster. Firstly, the cloud of the Carina Nebula is effectively blocking contaminating background objects. Furthermore, the effect of differential extinction should be lowered by the presence of the massive stars which removed the gas remaining from the star formation process such that highly reddened sources are unlikely to suffer from a large extinction. We identified 79 sources with infrared excess and 274 PMS stars without excess and, assuming all these stars to belong to the cluster, the fraction of excess sources would only amount to $\sim 22.5\%$, which is lower than the excess fraction of 35% as reported by Ascenso et al. (2007). Constraining the different regions of the CMD is in our case the best way to get a least biased view of the stellar population of Tr 14 and, subsequently, the best cluster LF.

5.2.2 K_S -band Luminosity Function

The LF is the number of stars as a function of magnitude. Stars are counted in magnitude bins of 0.5 mag, the counts are corrected for incompleteness and normalised to the considered area. The final K_S -band LF is shown in Fig. 8. The histogram displays the LF based on stars that belong to the PMS stars without excess (black dots in Fig. 7) and is not yet corrected for incompleteness. The completeness corrected LF is shown by the straight line with error bars that correspond to Poisson errors. The steep increase for stars fainter than $K_S \sim 16.5$ mag in the completeness corrected LF is due to the high incompleteness at the faint end. The dotted line further displays the LF of PMS stars including excess sources (black and grey dots in Fig. 7) and is corrected for incompleteness.

The LFs depict an increasing number of stars towards fainter magnitudes at the bright end until it turns over at $K_S = 14.75$ mag (PMS-LF) or $K_S = 15.25$ mag ('PMS+excess'-LF), respectively. This same turnover is also visible at $K_S \sim 15$ mag in the two K_S -LFs derived by Ascenso et al. (2007) based on NTT-SofI and VLT-NaCo observations, respectively.

Similar K -band LFs have been identified in clusters, observationally and by simulating model LFs of synthetic clusters (e.g. Zinnecker & McCaughrean 1991; Lada & Lada 2003). Zinnecker & McCaughrean (1991) simulated primarily K -band LFs for clusters of non-accreting PMS stars. They found time-dependent LFs exhibiting maxima that shift with time. Comparison of our LF with its maximum at $K_S \sim 14.75$ mag with the results of Zinnecker & McCaughrean (1991) reveal comparable functions for clusters between 0.7 and 1 Myr, consistent with the derived age for Tr 14. Such maxima are most likely caused by Deuterium-burning stars that lead to a peak in the LF. In a 1 Myr old cluster a PMS star of $0.3 M_{\odot}$ starts burning Deuterium, in

agreement with the masses that correspond to the observed peak in the LF.

5.3 Mass function

5.3.1 The Trumpler 14 Mass Function

The initial mass function (IMF) represents the distribution of stellar masses for a given stellar system at the time of its formation. The form of the MF changes with time due to stellar, as well as dynamical evolution. As a result of such evolutionary effects, which affect entire stellar systems such as star clusters (Baumgardt & Makino 2003), the MF is changed and, thus, the 'actual' MF will be called present-day mass function (PDMF). The PDMF is described, similar to the IMF, as a power law:

$$\Gamma_{\text{PD}} = \frac{d \log N(\log m)}{d \log m}, \quad (2)$$

where $N(\log m)$ is the PDMF. This slope is given by the linear relation between the logarithmic mass intervals and the corresponding number of stars (in logarithmic scale). With this notation the Salpeter-IMF has a slope of $\Gamma = -1.35$ (Salpeter 1955). Due to the youth of Tr 14, most of its members are populating the PMS which ends with the ignition of hydrogen in stellar cores at the MS turn-on. To obtain the mass of all PMS stars, we use the relation of the stellar luminosity and mass, the mass–luminosity relation (MLR), of the 1 Myr Siess isochrone. To convert apparent to absolute magnitudes we consider the distance of 2.3 ± 0.4 kpc and a constant foreground extinction of $A_{K_S} = 0.38 \pm 0.03$ mag as derived in Sect. 5.1. The mass of each star is estimated with the derived MLR and the corresponding magnitude. In case of the PMS stars without excess we have considered the brightness of the stars in K_S -band, as this minimises the effect of differential extinction. PMS stars with circumstellar material are, however, exhibiting an excess in the K_S -band. Therefore, we have used the H -band instead to reduce the effect of the excess when deriving the mass.

To obtain the PDMF of Tr 14, we use the method suggested by Maíz Apellániz & Úbeda (2005). They discuss the biases that are introduced by the binning process to derive the MF (see also Maíz Apellániz 2009). Assuming a constant bin size can lead to misleading results, due to the correlation between the number of stars per bin (higher for lower masses) and the assigned weights (from the Poisson statistics). To circumvent this problem they suggested a variable bin size to have an equal number of sources in each bin. They found, in this case, that the bias is almost independent on the assumed number of stars per bin, and remains low even for a single star in each bin.

To minimise the effect of the binning and to maintain the statistical information, we have chosen to derive the PDMF in single star bins. Therefore, we sort the stars of our catalogue by mass. Each 'bin' consists of a single star and its bin width is defined to be the mean of the star and the preceding and following star, respectively. For the most and least massive stars in the sample, the upper and lower boundaries of the bins are chosen to be symmetric from the actual mass of the star. The 'number' (1 by definition) of stars is corrected for incompleteness associated with the star and divided by the width of the bin.

The resulting PDMF is illustrated in Fig. 9. It displays two functions composed of *i)* only the PMS stars (index: PMS_i) and of *ii)* PMS stars and the 'excess' sources (index: all_i). In both cases, we identify a PDMF with a turnover at $\log(m) \sim -0.25$. The jump at $\log(m) \sim -0.6$ is due to a significant change in the slope of the MLR ($\sim 0.06 \text{ M}_\odot/\text{mag}$ for $m < 0.25 \text{ M}_\odot$ and $\sim 0.76 \text{ M}_\odot/\text{mag}$ for $m > 0.25 \text{ M}_\odot$). Therefore, and due to a probably increasing contribution of the Galactic field stars, the PDMF below $\log(m) < -0.6$ is not considered in the following fitting process. Thus, we fit a two-component power law with a variable characteristic mass in the mass range $0.25 < M < 3.2 \text{ M}_\odot$.

i) PDMF of PMS stars without excess sources (black dots in Fig. 7):

We find a characteristic mass of $m_c = 0.52^{+0.25}_{-0.17} \text{ M}_\odot$ and power law slopes of $\Gamma_{\text{PD,PMS1}} = -0.46 \pm 0.20$ above m_c and $\Gamma_{\text{PD,PMS2}} = 0.73 \pm 0.59$ below m_c .

ii) PDMF of PMS stars with excess sources (black and grey dots in Fig. 7):

We derived power law slopes of $\Gamma_{\text{PD,all1}} = -0.50 \pm 0.11$ and $\Gamma_{\text{PD,all2}} = 0.63 \pm 0.32$ above and below a turnover mass of $m_c = 0.53^{+0.12}_{-0.10} \text{ M}_\odot$, respectively. The slopes in both regimes agree very well within the fitting uncertainties. Consequently, no systematic bias is introduced due to the inclusion of excess sources and the derivation of the PDMF slope is independent of our cluster member selection. Therefore, when addressing the PDMF of Tr 14, we refer in the following to the PDMF including the excess sources, i.e. to $\Gamma_{\text{PD,all1}} = \Gamma_1 = -0.50 \pm 0.11$ and $\Gamma_{\text{PD,all2}} = \Gamma_2 = 0.63 \pm 0.32$ above and below $m_c = 0.53^{+0.12}_{-0.10} \text{ M}_\odot$.

The turnover mass that is identified agrees very well with the mass at which the flattening of the Kroupa–IMF occurs (Kroupa 2001). Such flattening of the MF around $\sim 0.53 \text{ M}_\odot$ is not an unique feature of Tr 14, but observed in other clusters (e.g. Fig. 3 in Bastian et al. 2010).

The slopes of the PDMF in the different mass regimes (above and below m_c , respectively) are notably shallower than the corresponding part of the Kroupa–IMF (Salpeter slope $\Gamma = -1.35$). However, a source of uncertainty in the derivation of the MF slope are unresolved binaries. Depending on the binary fraction and the intrinsic slope of the stellar MF, the observed slope may deviate from the intrinsic slope by up to $\Delta\Gamma \sim +0.5$ (e.g. Sagar & Richtler 1991; Kroupa 2001). Even with such a large correction our PDMF would appear flatter than a Kroupa–IMF.

Considering the rather flat slope of the PDMF of the central region of Tr 14 and the unaccounted effect of unresolved binaries, the derived PDMF is in good agreement with the central PDMFs observed in other young and massive clusters. In the very central region in NGC 3603 YC slopes of the MF are found between $\Gamma \sim -0.31$ and -0.91 , depending on the stellar population (MS, PMS, PMS plus MS) and area considered in deriving the MF (e.g. Sung & Bessell 2004; Stolte et al. 2006; Harayama et al. 2008). The different considered mass ranges do not hamper the comparison as above 0.5 M_\odot the MF is described by a single-power law (Salpeter 1955; Kroupa 2001). In the case of Westerlund 1, Gennaro et al. (2011) found a significant flattening of the PDMF towards the centre of the cluster with slopes down to $\Gamma \sim -0.7$ although the very centre could not be considered due to severe

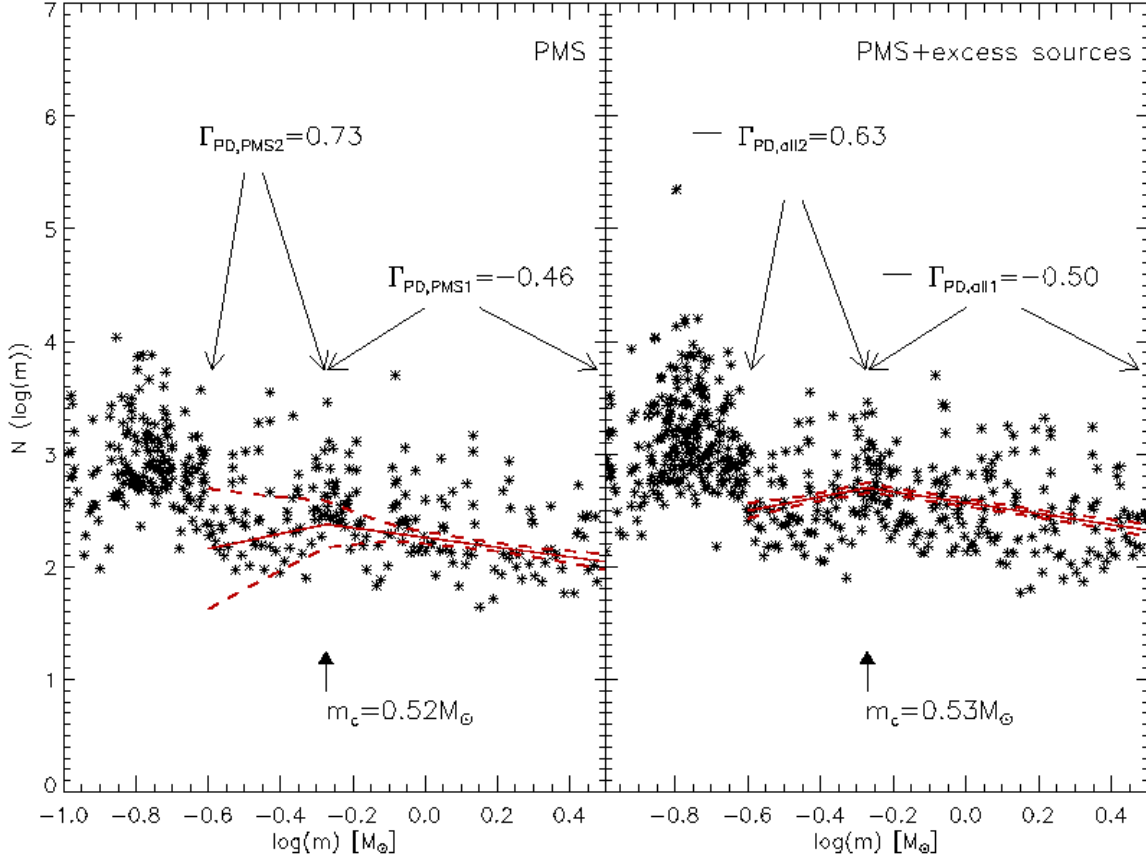


Figure 9. MF of Tr 14 derived following the suggested method of Maíz Apellániz & Úbeda (2005). Each 'bin' contains a single star, which has been corrected for incompleteness and is divided by the width of each bin. The two MFs are composed of stars of only the PMS (left panel) and of the PMS plus the 'excess' sources (right panel). The best fits to the MFs are shown as straight red lines while dashed lines display the 1σ interval. The 'high-mass' part is well represented by a power law with a slope of $\Gamma_{PD,PMS1} = -0.46 \pm 0.20$ (PMS) and $\Gamma_{PD,all1} = -0.50 \pm 0.11$ (PMS+'excess' sources). The 'intermediate' part appears increasing with stellar mass ($\Gamma_{PD,PMS2} = 0.73 \pm 0.59$ (PMS) and $\Gamma_{PD,all2} = 0.63 \pm 0.32$ (PMS+'excess' sources) with a turnover observed of $m_c = 0.52^{+0.25}_{-0.17} M_{\odot}$ (PMS) and $m_c = 0.53^{+0.12}_{-0.10} M_{\odot}$ (PMS+'excess' sources).

saturation effects. In the central 0.75 pc, as in our study of Tr 14, Brandner et al. (2008) could identify a similarly flat PDMF with $\Gamma \sim -0.5$.

However, it should be noted that we have to regard the effect of dynamical mass segregation in case of NGC 3603 YC and Westerlund 1 flattening the central PDMF because of the significantly higher density in these clusters. In contrast, no mass segregation was observed in the centre of Tr 14 in the considered mass range. Based on a minimum spanning tree analysis, mass segregation was identified for stars more massive than $10 M_{\odot}$ (Sana et al. 2010). They have analyzed the same MCAO data of Tr 14 but including also the shallower MAD observations of the adjacent fields, such that the analyzed FoV encloses the central 2 arcmin. A comparable result has been reported for the ONC with mass segregation above $5 M_{\odot}$ (Hillenbrand 1997; Allison et al. 2009). Allison et al. (2009) pointed out that the observed high-mass segregation can be of dynamical origin which can happen on very short time-scales of less than 1 Myr. The different degrees of segregation can be explained by the higher density of the ONC (about 15 times that of Tr 14) reducing the time-scales

on which mass segregation occurs. In conclusion, a shallow PDMF as we observe in Tr 14 is not an uncommon feature but observed in several massive young clusters, but its origin remains elusive.

5.3.2 'Traditional' Mass Function

For comparison, we construct the PDMF also in the 'traditional' way, counting stars in logarithmic mass intervals with $\Delta \log(m) = 0.2$ dex and $\Delta \log(m) = 0.1$ dex. Stars are counted in each bin and normalised to the considered area. The results are corrected for incompleteness and the resulting PDMFs are shown in Fig. 10. Above $0.5 M_{\odot}$, we fitted single-power law with the data points weighted by the individual Poisson errors. The corresponding slopes of are summarised in Table 2. The derived power law slopes agree within the errors with the PDMF of Fig. 9, although the PDMFs with 0.1 dex spacing appear steeper. Towards lower masses we also identify the drop of the mass function below $0.5 M_{\odot}$ followed by a steep increase below $0.25 M_{\odot}$. Due

Table 2. Slopes of the different mass functions

Mass range M_{\odot}	Binning	$\Gamma_{\text{PD,PMS}}$	$\sigma_{\Gamma_{\text{PD,PMS}}}$	$\Gamma_{\text{PD,all}}$	$\sigma_{\Gamma_{\text{PD,all}}}$
$m_c - 3.2$	1 star	-0.46	0.20	-0.50	0.11
	0.1 dex	-0.70	0.31	-0.60	0.26
	0.2 dex	-0.59	0.27	-0.52	0.30
$0.25 - m_c$	1 star	0.73	0.59	0.63	0.32

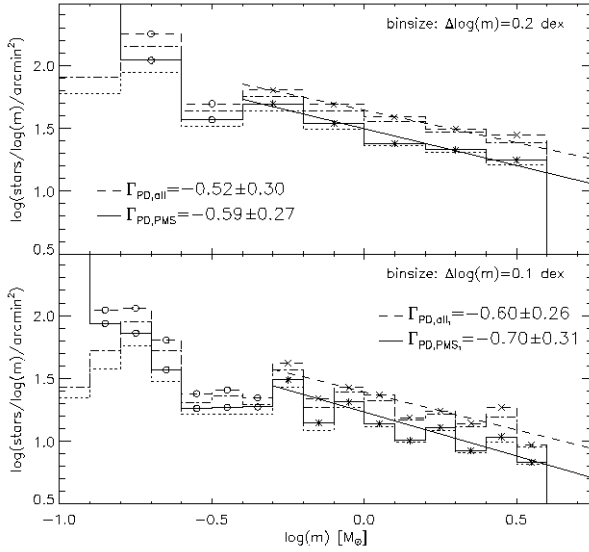


Figure 10. MFs of Tr 14 derived with the ‘traditional’ method. *Upper Panel:* The PDMF through star counts with bins of $\Delta \log(m) = 0.2$ dex. Above $0.5 M_{\odot}$ we find $\Gamma_{\text{PD,PMS}} = -0.59 \pm 0.27$ and $\Gamma_{\text{PD,all}} = -0.52 \pm 0.30$. *Lower Panel:* The PDMF obtained via star counts with a bin size of $\Delta \log(m) = 0.1$ dex. Above $0.5 M_{\odot}$ we derive similar slopes as for the 0.2 dex-bins ($\Gamma_{\text{PD,PMS}_1} = -0.70 \pm 0.31$ and $\Gamma_{\text{PD,all}_1} = -0.60 \pm 0.26$).

to the sparsity of data points, we have not fitted the PDMF below $0.5 M_{\odot}$.

6 SUMMARY

We presented deep H and K_S observations of the young massive cluster Tr 14, observed with MAD, the first MCAO system at the VLT.

i) MAD (MCAO) in crowded regions:

We revealed an impressive performance of the AO system over a large FoV. As part of the technical analysis we derived maps of Strehl ratios which show a low variation over the $68 \text{ arcsec} \times 68 \text{ arcsec}$ FoV. Mean Strehl values are measured to 6.0 and 5.9 per cent in H - and K_S -band, respectively. Simulating SCAO observations over the same FoV revealed smaller mean Strehls (1.6 per cent in H and 2.0 per cent in K_S). Although with lower maximum Strehl ratios (9.8 per cent in H -band, 12.6 per cent in K_S -band), when compared to SCAO systems, this shows a significant improvement of the spatial stability of the AO performance

and demonstrates the opportunities offered by MCAO systems for wide-field AO corrected observations.

PSF photometry has been applied to derive properties of Tr 14. The results show that the photometry is well estimated by using a second order variable PSF (see also Sana et al. 2010). Photometric calibration was accomplished using seeing-limited NTT-SofI observations (Ascenso et al. 2007). A spatially constant ZP offset was found when compared to seeing-limited observations and used for photometric calibration. The resulting photometric catalogue comprises 972 (1347) sources down to very-low mass ($\lesssim 0.1 M_{\odot}$) PMS stars. This doubles (triples) the number of detections when compared to seeing-limited observations of the same field.

ii) K_S vs. $H - K_S$ CMD of Tr 14:

The photometric catalogue with almost 1,000 sources was used to create a K_S vs. $H - K_S$ CMD of Tr 14. It reveals a clear sequence of PMS stars, dozens of ‘excess’ sources and a sparsely populated MS. Comparing the CMD with PMS tracks by Siess et al. (2000), we find the CMD is best represented by an isochrone of 1 ± 0.5 Myr in age while hints for a somewhat older PMS population are observable. This places Tr 14 at a distance of 2.3 ± 0.4 kpc with a foreground extinction of $A_{K_S} = 0.38 \pm 0.03$ mag ($A_V = 3.0 \pm 0.4$ mag). Hints for star formation over the last 3 Myr support earlier claims of continuous star formation in the region and a slightly older halo population of the cluster (e.g. Ascenso et al. 2007).

iii) The LF and MF:

The LF of Tr 14 is derived based on the K_S magnitudes. The observed turnover at $K_S = 14.75$ mag is consistent with a cluster of the derived age of ~ 1 Myr and the limiting mass at which Deuterium burning ceases.

We derived the PMS stellar PDMF that appears to be well represented by a broken power law between 0.25 and $3.2 M_{\odot}$. We found a PDMF that shows a change of the power law slope at $m_c = 0.53 M_{\odot}$ comparable to that of a Kroupa-IMF. Such variations of the MF (flattening, turnover) of stellar systems are observed in other young clusters at similar stellar mass. The corresponding power law slopes, however, show a shallower PDMF when compared to the Kroupa-IMF (Salpeter slope $\Gamma = -1.35$). In the intermediate- and low-mass regime we find slopes of $\Gamma_1 = -0.50 \pm 0.11$ above m_c and $\Gamma_2 = 0.63 \pm 0.32$ below m_c down to $\sim 0.25 M_{\odot}$. This reveals a deficiency in low-mass stars in the centre of Tr 14. Furthermore, comparison with other young massive clusters shows similarly shallow PDMFs in the centres of young and massive clusters.

This study reveals the great improvement of AO corrections provided by MCAO systems in the case of wide field AO corrected observations. The stability of the correction

for atmospheric turbulence in combination with the correction over a few arcminutes provides an ideal combination for investigations that depend on high spatial resolution instruments as well as a large FoV. Therefore, VLT–MAD gives a very promising impression of the future prospects of observations with upcoming new telescopes and instruments.

ACKNOWLEDGMENTS

Our thanks go to the referee for the very constructive comments and discussion of our work leading to subsequent improvements of the paper. We would like to acknowledge the support by the Deutsches Zentrum für Luft- und Raumfahrt (DLR), Förderkennzeichen 50 OR 0401 and the German Research Foundation (DFG) through the Emmy Noether grant STO 496/3-1.

REFERENCES

- Allard F., Freytag B. 2010, *Highlights of Astronomy*, 15, 756
- Allison R. J., Goodwin S. P., Parker R. J., de Grijs R., Portegies Zwart S. F., Kouwenhoven M. B. N. 2009, *ApJ*, 700, L99
- Amorim A., et al. 2006, *Proc. SPIE*, 6269,
- Ascenso J., Alves J., Vicente S., Lago M. T. V. T. 2007, *A&A*, 476, 199
- Baraffe, I., Chabrier, G., Allard, F., & Hauschildt, P. H. 2002, *A&A*, 382, 563
- Bastian N., Covey K. R., Meyer M. R. 2010, *ARA&A*, 48, 339
- Baumgardt H., Makino J. 2003, *MNRAS*, 340, 227
- Bertin E., Arnouts S. 1996, *A&AS*, 117, 393
- Brandner W., Clark J. S., Stolte A., Waters R., Negueruela I., Goodwin S. P. 2008, *A&A*, 478, 137
- Campbell M. A., Evans C. J., Mackey A. D., Gieles M., Alves J., Ascenso J., Bastian N., Longmore A. J. 2010, *MNRAS*, 405, 421
- Cardelli J. A., Clayton G. C., Mathis J. S. 1989, *ApJ*, 345, 245
- Carraro G., Romaniello M., Ventura P., Patat F. 2004, *A&A*, 418, 525
- Cresci G., Davies R. I., Baker A. J., Lehnert M. D. 2005, *A&A*, 438, 757
- Da Rio, N. Gouliermis D. A., Henning T., 2009, *ApJ*, 696, 528
- Devillard N. 2001, *Astronomical Data Analysis Software and Systems X*, 238, 525
- Gennaro M., Brandner W., Stolte A., Henning T. 2011, *MNRAS*, 162
- Harayama Y., Eisenhauer F., Martins F. 2008, *ApJ*, 675, 1319
- Hillenbrand L. A. 1997, *AJ*, 113, 1733
- Kroupa P. 2001, *MNRAS*, 322, 231
- Lada C. J., Lada E. A. 2003, *ARA&A*, 41, 57
- Maíz Apellániz J., & Úbeda L. 2005, *ApJ*, 629, 873
- Maíz Apellániz J. 2009, *Ap&SS*, 324, 95
- Marchetti E., Ragazzoni R., Diolaiti E. 2003, *Proc. SPIE*, 4839, 566
- Marchetti E., et al. 2004, *Proc. SPIE*, 5490, 236
- Marchetti E., et al. 2007, *The Messenger*, 129, 8
- Marigo P., Girardi L., Bressan A., Groenewegen M. A. T., Silva L., Granato G. L. 2008, *A&A*, 482, 883
- Massey P., Johnson J. 1993, *AJ*, 105, 980
- Momany Y., Ortolani S., Bonatto C., Bica E., Barbuy B. 2008, *MNRAS*, 391, 1650
- Naylor T. 2009, *MNRAS*, 399, 432
- Nelan E. P., Walborn N. R., Wallace D. J., Moffat A. F. J., Makidon R. B., Gies D. R., Panagia N. 2004, *AJ*, 128, 323
- Rathborne J. M., Burton M. G., Brooks K. J., Cohen M., Ashley M. C. B., Storey J. W. V. 2002, *MNRAS*, 331, 85
- Rochau B., Brandner W., Stolte A., Gennaro M., Gouliermis D., Da Rio N., Dzyurkevich N., Henning T. 2010, *ApJ*, 716, L90
- Rousset G., Fontanella J. C., Kern P., Gigan P., Rigaut F. 1990, *A&A*, 230, L29
- Sagar R., Richtler T. 1991, *A&A*, 250, 324
- Salpeter E. E. 1955, *ApJ*, 121, 161
- Sana H., Momany Y., Gieles M., Carraro G., Beletsky Y., Ivanov V. D., de Silva G., James G. 2010, *A&A*, 515, A26
- Siess L., Dufour E., Forestini M., 2000, *A&A*, 358, 593
- Smith N. 2006, *MNRAS*, 367, 763
- Stetson P. B., 1990, *PASP*, 102, 932
- Stolte A., Grebel E. K., Brandner W., Figer D. F. 2002, *A&A*, 394, 459
- Stolte A., Brandner W., Brandl B., Zinnecker H. 2006, *AJ*, 132, 253
- Sung H., Bessell M. S. 2004, *AJ*, 127, 1014
- Tapia M., Roth M., Vázquez R. A., Feinstein A. 2003, *MNRAS*, 339, 44
- Vazquez R. A., Baume G., Feinstein A., Prado P. 1996, *A&AS*, 116, 75
- Walborn, N. R., et al. 2002, *AJ*, 123, 2754
- Zinnecker H., McCaughrean M. 1991, *Mem. Soc. Astron. Italiana*, 62, 761